LETTER

doi:10.1038/nature14872

Substitutional doping in nanocrystal superlattices

Matteo Cargnello[1]*†, Aaron C. Johnston-Peck[2]*, Benjamin T. Diroll[1]*, Eric Wong[3], Bianca Datta[4], Divij Damodhar[4], Vicky V. T. Doan-Nguyen[4], Andrew A. Herzing[2], Cherie R. Kagan[1,4,5] & Christopher B. Murray[1,4]

Doping is a process in which atomic impurities are intentionally added to a host material to modify its properties. It has had a revolutionary impact in altering or introducing electronic[1,2], magnetic[3,4], luminescent[5,6], and catalytic[7] properties for several applications, for example in semiconductors. Here we explore and demonstrate the extension of the concept of substitutional atomic doping to nanometre-scale crystal doping, in which one nanocrystal is used to replace another to form doped self-assembled superlattices. Towards this goal, we show that gold nanocrystals act as substitutional dopants in superlattices of cadmium selenide or lead selenide nanocrystals when the size of the gold nanocrystal is very close to that of the host. The gold nanocrystals occupy random positions in the superlattice and their density is readily and widely controllable, analogous to the case of atomic doping, but here through nanocrystal self-assembly. We also show that the electronic properties of the superlattices are highly tunable and strongly affected by the presence and density of the gold nanocrystal dopants. The conductivity of lead selenide films, for example, can be manipulated over at least six orders of magnitude by the addition of gold nanocrystals and is explained by a percolation model. As this process relies on the self-assembly of uniform nanocrystals, it can be generally applied to assemble a wide variety of nanocrystal-doped structures for electronic, optical, magnetic, and catalytic materials.

Wet chemical methods can produce ensembles of monodisperse colloidal nanocrystals[8] (in which the particles are of very similar size), with sizes that can be controlled with subnanometre precision[9]. These uniform nanocrystals can self-assemble into periodic superlattices that have the same crystal structure as atomic and molecular crystals[10], with great potential for several applications[11]. Higher complexity can be obtained when two (or more) sets of monodisperse particles with different sizes or shapes are assembled into binary nanocrystal superlattices (BNSLs) with tunable stoichiometry and crystal structure[12]. These metamaterials show emergent properties that are derived from the nanoscale interactions between the building blocks, which can be chosen from many sizes, shapes, and chemical compositions[13]. However, in BNSLs—as in binary compounds—the stoichiometry and crystal structure are interdependent and are constrained by the specific particle sizes and size ratios.

In contrast to BNSLs, in which the size difference is the driving force for the ordered assembly, two sets of monodisperse nanocrystals with very similar sizes should produce assemblies in which the two components randomly occupy the same sites of a superlattice, thus achieving substitutional doping of the superlattice. We explore this hypothesis by preparing monodisperse gold (Au) and cadmium selenide (CdSe) nanocrystals that have similar (roughly 5.5-nm) diameter (excluding the organic ligands) and size dispersions smaller than 6%, which means that each nanocrystal differs from another by no more than 6% of its size (Extended Data Fig. 1). In this method, Au and CdSe nanocrystal dispersions in hexane are mixed and allowed to self-assemble on a diethylene glycol surface according to a well developed liquid–air interface method[14]. Ordered nanocrystal monolayers are initially targeted, because of their simplicity relative to thick superlattices, for an unambiguous structural characterization of the doped films.

A representative high-angle annular dark-field scanning transmission electron microscopy (HAADF-STEM) image of an Au-nanocrystal-doped CdSe nanocrystal monolayer is shown in Fig. 1A, revealing that ordered, hexagonal close-packed arrays are formed. Owing to the large difference in atomic number between Au ($Z = 79$) and Cd ($Z = 48$), Au nanocrystals appear much brighter than CdSe nanocrystals under HAADF-STEM, while the image contrast is the opposite in bright-field transmission electron microscopy (TEM) mode (Fig. 1B). Superlattice monolayers extend to several square micrometres in area. It is evident at high magnification that local hexagonal packing is maintained and that no point defects are introduced by the Au nanocrystal dopants (Fig. 1B, C and Extended Data Fig. 2). To unequivocally demonstrate the presence and location of Au nanocrystals, we correlate energy-dispersive X-ray spectroscopy (EDS) compositional maps and HAADF-STEM images of the Au–CdSe nanocrystal monolayers (Fig. 1Fa–d). Imaging of high-contrast particles in HAADF-STEM (Fig. 1Fa) reveals that lower-contrast particles are composed of Cd and Se (Fig. 1Fb) and that the bright spots are well correlated with the EDS map of Au nanocrystals (Fig. 1Fc).

The density of the dopant Au nanocrystals in the monolayer superlattices can be tuned by varying the concentration of these nanocrystals in the starting dispersions used for self-assembly. Extended Data Fig. 3a–d shows monolayers prepared with Au nanocrystal densities of 66 μm^{-2}, 128 μm^{-2}, 183 μm^{-2} and 317 μm^{-2}—densities that are in good accordance with the Au/CdSe ratios used in our starting solutions (see Methods for details). To assess the randomness of the process, we carried out a Voronoi analysis on the images, removing the edges, resulting in tessellations similar to that shown in Fig. 1D. The results, averaged over at least 25 different TEM images for each of the samples with the Au densities mentioned above, are shown as histograms in Fig. 1E and Extended Data Fig. 3e–g. The average particle–particle distance decreases with increasing Au density, varying from 46 nm to 41 nm to 37 nm to 25 nm. The histograms showing the distributions of Au particle–particle distances are well described by a log-normal distribution, indistinguishable from a gamma distribution, as would be expected for a random tessellation[15]. The average number of edges is very close to six for all the samples. Thus the Voronoi analysis demonstrates that the Au particles behave as random substitutional dopants.

To achieve a truly random mixing of Au nanocrystals in the CdSe superlattice, the two particles must have similar size and show favourable enthalpic contributions to mixing, obtained mainly through the chemistry of their surface ligands. The successful incorporation of Au nanocrystal dopants is realized using 1-dodecanethiol ligands. Au nanocrystals that were coated with oleylamine, but otherwise of the same size as the CdSe nanocrystals, segregated to the grain boundaries rather than being incorporated into the grains (Extended Data Fig. 4).

[1]Department of Chemistry, University of Pennsylvania, Philadelphia, Pennsylvania 19104, USA. [2]Material Measurement Laboratory, National Institute of Standards and Technology, Gaithersburg, Maryland 20899, USA. [3]Department of Physics, University of Pennsylvania, Philadelphia, Pennsylvania 19104, USA. [4]Department of Materials Science and Engineering, University of Pennsylvania, Philadelphia, Pennsylvania 19104, USA. [5]Department of Electrical and Systems Engineering, University of Pennsylvania, Philadelphia, Pennsylvania 19104, USA. †Present address: Department of Chemical Engineering and SUNCAT Center for Interface Science and Catalysis, Stanford University, Stanford, California 94305, USA.
*These authors contributed equally to this work.

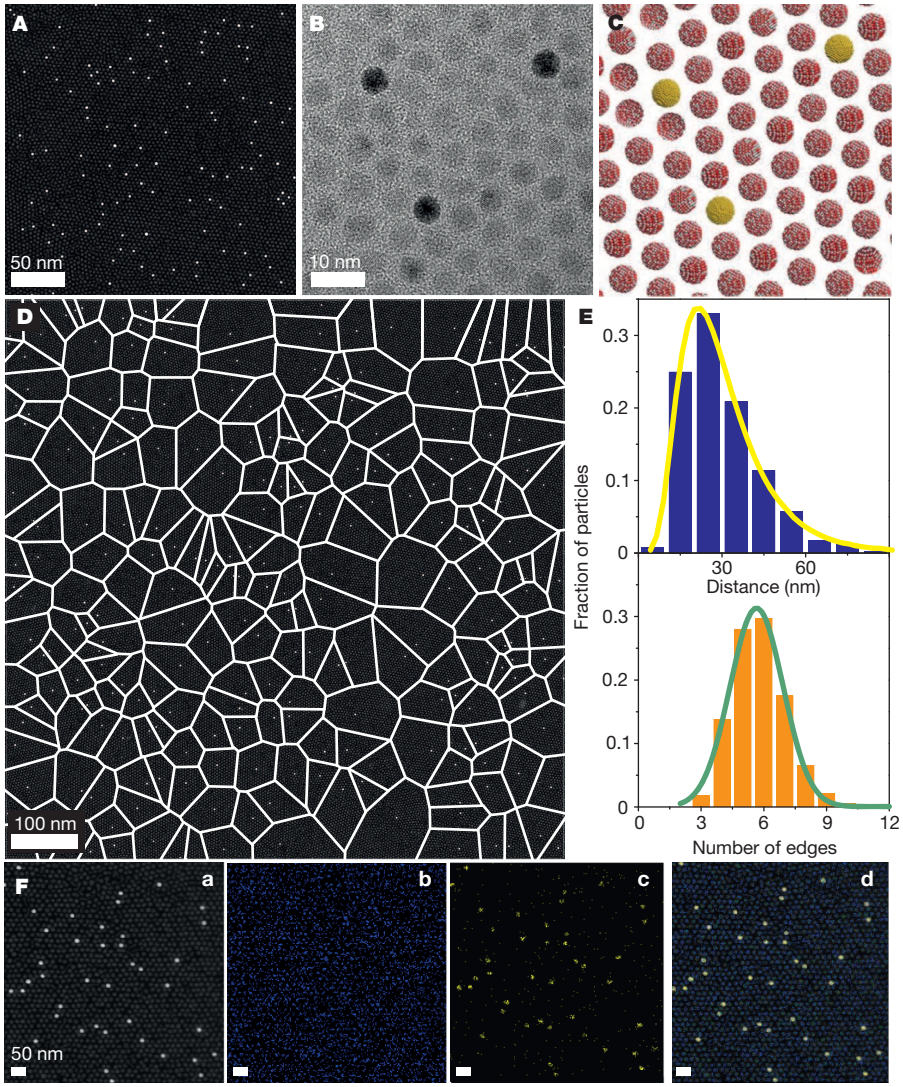

Figure 1 | Characterization of doped monolayer superlattices. **A**, **B**, Representative HAADF-STEM and TEM images of a CdSe nanocrystal monolayer doped with Au nanocrystals. The Au nanocrystals are seen as bright spots in **A** and dark spots in **B**. **C**, Model of the doped layer, showing the presence of Au nanocrystals (yellow) in the ordered superlattice of CdSe nanocrystals (red/grey). **D**, Voronoi diagram (white) on top of an HAADF-STEM image; Au nanocrystals are visible as small, bright dots. **E**, Histograms showing the distances between Au nanocrystals (top) and the number of edges for polygons in the Voronoi analysis (bottom); $N = 227$. **F**, **a**, HAADF-STEM mapping of an Au–CdSe nanocrystal monolayer. **b**, EDS mapping of Cd. **c**, EDS mapping of Au. **d**, Overlay EDS image.

We attribute this behaviour to the slight difference in ligand length (0.95 nm for oleylamine; 0.85 nm for dodecanethiol), the larger Hamaker constant of Au (which would dictate a more favourable interaction between Au nanocrystals[16]), and the instability of Au nanocrystals coated with oleylamine at the liquid–air interface. However, additional detailed studies are required to complete the explanation for this behaviour.

To further understand the mechanism of dopant incorporation into the lattice, we looked at the co-assembly of the same Au nanocrystals with the slightly larger (6.5-nm) lead selenide (PbSe) nanocrystals. Here, almost exclusive phase separation of the Au nanocrystals occurs, regardless of the ligand chosen for Au stabilization (Extended Data Fig. 5). Given that the deposition conditions for nanocrystal superlattice assembly and the Hamaker constants are similar for different chalcogenides (such as CdSe and PbSe), we attribute the segregation of Au nanocrystals in PbSe layers instead to size mismatch. Au nanocrystals would in fact introduce distortions into the PbSe nanocrystal superlattice, making it unfavourable. For this reason, dopants become excluded and collect together where the strain is released, for example at grain boundaries, in a process that is comparable to grain-boundary segregation of ions of different sizes in atomic-scale systems[17]. In accordance with these observations, we find that the co-assembly of slightly larger (6.8-nm) nanocrystals that consist of a gold core and a silver shell (Au/Ag) with the PbSe nanocrystals results in superlattices with long-range order, as seen for the Au–CdSe combination (Extended Data Fig. 6).

We prepared thicker films with uniform and tunable doping density by increasing the concentration of both particles in the starting solutions, resulting in ordered multilayers with Au or Au/Ag nanocrystals dispersed within the CdSe or PbSe nanocrystal superlattices (Fig. 2). High-resolution HAADF-STEM again clearly distinguishes bright Au/Ag nanocrystals that are well dispersed within three-dimensional superlattices of PbSe nanocrystals (Fig. 2a, b)[18]. We observe that Au nanocrystals are preferentially incorporated into multilayer regions (Extended Data Fig. 7), probably because of unfavourable interactions between these nanocrystals and the liquid subphase used for the assembly process. Further investigation is needed to understand this observation. Transmission small-angle X-ray scattering (TSAXS) patterns show the presence of six intense spots offset by 60°, consistent with the close-packed plane of the nanocrystal superlattice, and demonstrating that the order of a single superlattice is maintained over at least 50 μm (Fig. 2c). TEM tomography measurements on the exchanged films show that the Au/Ag dopants are dispersed throughout the superlattice volume and do not segregate to the top surface. A reconstruction of about 10^7 nm^3 is shown in Fig. 2d, together with side and top views (Fig. 2d–f and Supplementary Video), illustrating the random dispersion of the Au nanocrystals along the z axis of the films.

The presence and density of Au nanocrystal dopants drastically modifies the electronic properties of semiconductor nanocrystal superlattices. To improve the coupling between the nanocrystals[19], we displaced the long, insulating, aliphatic ligands with the more compact thiocyanate anion (SCN^-) through a two-step procedure that

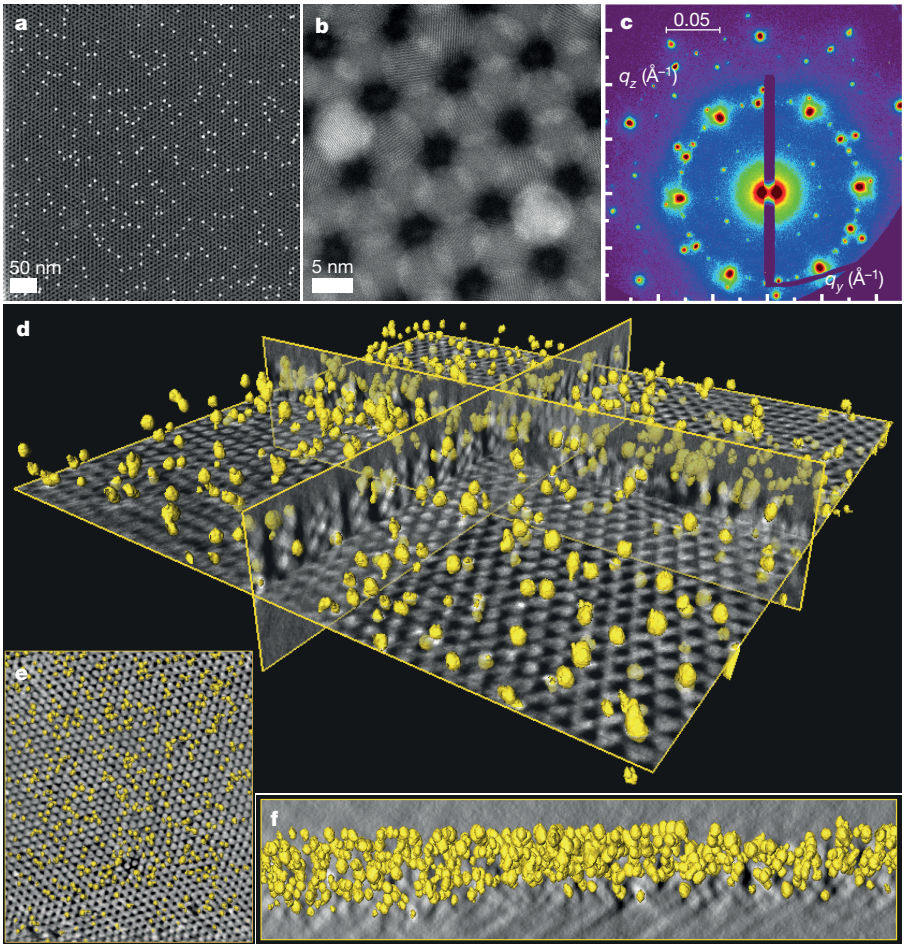

Figure 2 | Characterization of doped multilayered superlattices. **a**, **b**, HAADF-STEM images of multilayer films of Au/Ag–PbSe nanocrystals. **c**, The corresponding TSAXS pattern shows scattered intensity along the q_z and q_y vectors. **d**, Tomographic reconstruction of a portion of the multilayer films in which Au nanocrystals (yellow spheres) are highlighted, with **e** and **f** showing the *YZ* and *XY* slice views of the same region, respectively.

preserves the superlattice structure[20]. Microscopy studies demonstrate that, despite the decrease in the interparticle distance, the superlattices remain intact (Extended Data Fig. 8). Furthermore, marked atomically coherent interfaces between nanocrystals are not observed in the electron-diffraction patterns of selected areas (Extended Data Fig. 8c)[18]. We studied the electrical conductivity of PbSe nanocrystal films doped with Au/Ag nanocrystals by laminating films on patterned substrates (Extended Data Fig. 9). Current–voltage (*I*–*V*) curves (Fig. 3a) show that the direct-current conductivity (σ) is modulated by more than six orders of magnitude, from $\sigma = 6.7 \times 10^{-6}$ S cm^{-1} for pure PbSe nanocrystals, to $\sigma = 7.05$ S cm^{-1} for 16.5% Au/Ag-doped PbSe superlattices (Fig. 3b). Unlike the situation that occurs with classical doping in microelectronics, modulation in the conductivity of the PbSe nanocrystal superlattice is achieved not by ionization of the Au/Ag dopant, but by percolation (described below). Other nanocrystal inclusions within superlattices may allow classical 'doping' through thermal ionization to yield n- or p-type materials.

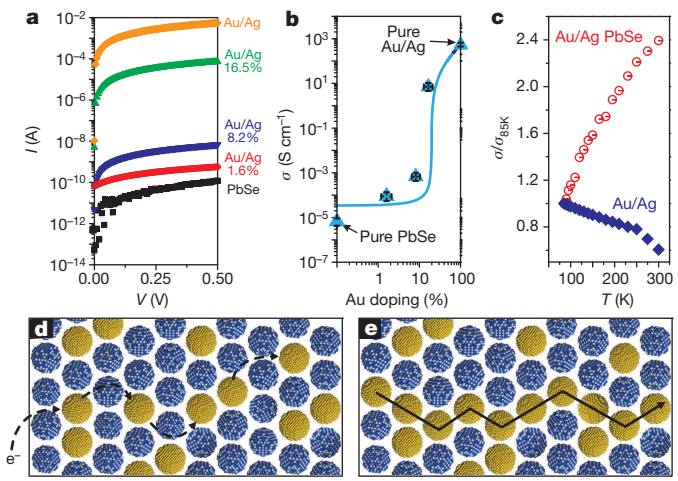

Figure 3 | Direct-current conductivity characterization of PbSe nanocrystal superlattices doped with varying amounts of Au/Ag nanocrystals. **a**, *I*–*V* curves, and **b**, conductivity of the nanocrystal superlattices as a function of Au/Ag doping. The blue curve in **b** shows the expectations of the Efros–Shklovskii percolation model[21]. **c**, Temperature-dependent conductivity of films of PbSe superlattices doped with 16.5% Au/Ag nanocrystals (red), and films of pure Au/Ag nanocrystals (blue). **d**, **e**, Schematics showing conductivity in systems below (**d**) and above (**e**) the percolation threshold in a honeycomb lattice showing the hopping path for electrons in **d** (dashed black arrow) and the direct electron transfer between Au nanocrystals in **e** (filled black arrow). The error bars in **b** show the standard deviation of 12 measurements.

The observed doping dependence of conductivity in Au/Ag-doped PbSe nanocrystal superlattices follows the classical behaviour observed for percolation in a random metal–dielectric composite (blue line in Fig. 3b)[21]. Percolation models predict a piecewise function to model conductivity, divided into three regions of compositional space:

$$\sigma(x) = \begin{cases} \sigma_m (x - x_c)^t & \text{if } x > x_c \\ \sigma_m \left(\dfrac{\sigma_D}{\sigma_M}\right)^s & \text{if } x = x_c \\ \sigma_d (x_c - x)^{-q},\ q > 0 & \text{if } x < x_c \end{cases}$$

where x is the concentration of metal, x_c is the site percolation threshold (19.5% for hexagonal close-packed and face-centred cubic arrangements[22]), σ_m and σ_d are the conductivities of the metal and dielectric constituents respectively, and t, s, and q are exponential factors that depend on the dimensionality of the system but have no precise definition in three dimensions. The large increase of

conductivity seen when doping approaches 20% is also indicative of the superlattice structure, which has a lower percolation threshold than that of glassy systems with fewer near-neighbours[23].

To investigate the microstructure of the doped superlattice further, we carried out temperature-dependent conductivity measurements of the 16.5% doping and the pure Au/Ag samples. For the 16.5% doping sample, the best single fit over the entire temperature range is a modified form of Efros–Shklovskii variable-range hopping, in which the conductivity is $\ln[\sigma(T)] \propto T^{-2/3}$ (Fig. 3c and Extended Data Fig. 10), similar to the conductivity observed for Au nanocrystal solids linked with alkane dithiols that have more than five carbons[24,25]. The observation of this behaviour in sub-percolation doped superlattices is expected, because conductivity is constrained by hopping beyond nearest neighbours. In contrast, pure Au/Ag nanocrystal films show non-activated, metallic conductivities that increase at lower temperatures over the entire temperature range of this study (Fig. 3c), similar to the conductivities observed for Au nanocrystal films with dithiol spacers with fewer than five carbons[25], for chemically exchanged Au nanocrystals[26] or for carbon-nanotube-doped organic semiconductors[27].

In much the same way that atomic doping is essential for applications using atomic solids, we expect nanocrystal doping to show promise in many areas. The compositional variety of colloidal nanocrystals and the versatility of the self-assembly provide a way to modulate optical, magnetic, structural, and electrical properties of nanocrystal superlattices via substitutional doping. Because nanocrystals can be combined arbitrarily[28], they offer the possibility of generating composite solids with combinations of properties that are not achievable either in the bulk superlattice or in previously described binary assemblies. It is also notable that substantially diluted nanocrystal superlattice systems can be produced without losing periodicity.

Online Content Methods, along with any additional Extended Data display items and Source Data, are available in the online version of the paper; references unique to these sections appear only in the online paper.

Received 15 May; accepted 26 June 2015.

1. Erwin, S. C. *et al.* Doping semiconductor nanocrystals. *Nature* **436,** 91–94 (2005).
2. Norris, D. J., Efros, A. L. & Erwin, S. C. Doped nanocrystals. *Science* **319,** 1776–1779 (2008).
3. Pearton, S. J. *et al.* Wide band gap ferromagnetic semiconductors and oxides. *J. Appl. Phys.* **93,** 1–13 (2003).
4. Röder, H., Zang, J. & Bishop, A. R. Lattice effects in the colossal-magnetoresistance manganites. *Phys. Rev. Lett.* **76,** 1356–1359 (1996).
5. Wang, F. *et al.* Simultaneous phase and size control of upconversion nanocrystals through lanthanide doping. *Nature* **463,** 1061–1065 (2010).
6. Ye, X. *et al.* Morphologically controlled synthesis of colloidal upconversion nanophosphors and their shape-directed self-assembly. *Proc. Natl Acad. Sci. USA* **107,** 22430–22435 (2010).
7. Asahi, R. *et al.* Visible-light photocatalysis in nitrogen-doped titanium oxides. *Science* **293,** 269–271 (2001).
8. Murray, C. B., Norris, D. J. & Bawendi, M. G. Synthesis and characterization of nearly monodisperse CdE (E = S, Se, Te) semiconductor nanocrystallites. *J. Am. Chem. Soc.* **115,** 8706–8715 (1993).
9. Park, J. *et al.* One-nanometer-scale size-controlled synthesis of monodisperse magnetic iron oxide nanoparticles. *Angew. Chem. Int. Ed.* **44,** 2872–2877 (2005).
10. Pileni, M. P. Self organization of inorganic nanocrystals: unexpected chemical and physical properties. *J. Colloid Interf. Sci.* **388,** 1–8 (2012).
11. Talapin, D. V., Lee, J. S., Kovalenko, M. V. & Shevchenko, E. V. Prospects of colloidal nanocrystals for electronic and optoelectronic applications. *Chem. Rev.* **110,** 389–458 (2010).
12. Shevchenko, E. V. *et al.* Structural diversity in binary nanoparticle superlattices. *Nature* **439,** 55–59 (2006).
13. Urban, J. J. *et al.* Synergism in binary nanocrystal superlattices leads to enhanced p-type conductivity in self-assembled PbTe/Ag_2Te thin films. *Nature Mater.* **6,** 115–121 (2007).
14. Dong, A. *et al.* Binary nanocrystal superlattice membranes self-assembled at the liquid–air interface. *Nature* **466,** 474–477 (2010).
15. Tanemura, M. Statistical distributions of Poisson Voronoi cells in two and three dimensions. *Forma* **18,** 221–247 (2003).
16. Bodnarchuk, M. I., Kovalenko, M. V., Heiss, W. & Talapin, D. V. Energetic and entropic contributions to self-assembly of binary nanocrystal superlattices: temperature as the structure-directing factor. *J. Am. Chem. Soc.* **132,** 11967–11977 (2010).
17. Meledina, M. *et al.* Local environment of Fe dopants in nanoscale Fe: CeO_{2-x} oxygen storage material. *Nanoscale* **7,** 3196–3204 (2015).
18. Boneschanscher, M. P. *et al.* Long-range orientation and atomic attachment of nanocrystals in 2D honeycomb superlattices. *Science* **344,** 1377–1380 (2014).
19. Fafarman, A. T. *et al.* Thiocyanate-capped nanocrystal colloids: vibrational reporter of surface chemistry and solution-based route to enhanced coupling in nanocrystal solids. *J. Am. Chem. Soc.* **133,** 15753–15761 (2011).
20. Dong, A., Jiao, Y. & Milliron, D. J. Electronically coupled nanocrystal superlattice films by *in situ* ligand exchange at the liquid–air interface. *ACS Nano* **7,** 10978–10984 (2013).
21. Efros, A. L. & Shklovskii, B. I. Critical behaviour of conductivity and dielectric constant near the metal-non-metal transition threshold. *Phys. Status Solid. B* **76,** 475–485 (1976).
22. Lorenz, C. D., May, R. & Ziff, R. M. Similarity of percolation thresholds on the HCP and FCC lattices. *J. Stat. Phys.* **98,** 961–970 (2000).
23. Rintoul, M. D. & Torquato, S. Precise determination of the critical threshold and exponents in a three-dimensional continuum percolation model. *J. Phys. Math. Gen.* **30,** L585 (1997).
24. Houtepen, A. J., Kockmann, D. & Vanmaekelbergh, D. Reappraisal of variable-range hopping in quantum-dot solids. *Nano Lett.* **8,** 3516–3520 (2008).
25. Zabet-Khosousi, A. *et al.* Metal to insulator transition in films of molecularly linked gold nanoparticles. *Phys. Rev. Lett.* **96,** 156403 (2006).
26. Fafarman, A. T. *et al.* Chemically tailored dielectric-to-metal transition for the design of metamaterials from nanoimprinted colloidal nanocrystals. *Nano Lett.* **13,** 350–357 (2013).
27. Bo, X. Z. *et al.* Carbon nanotubes-semiconductor networks for organic electronics: the pickup stick transistor. *Appl. Phys. Lett.* **86,** 1–3 (2005).
28. Overgaag, K., Liljeroth, P., Grandidier, B. & Vanmaekelbergh, D. Scanning tunneling spectroscopy of individual PbSe quantum dots and molecular aggregates stabilized in an inert nanocrystal matrix. *ACS Nano* **2,** 600–606 (2008).

Supplementary Information is available in the online version of the paper.

Acknowledgements We thank Y. Lai and D. Straus (University of Pennsylvania) for discussions about electrical characterization. This work received primary support from the Office of Naval Research MURI program (award number ONR-N00014-10-1-0942) for the development of the multicomponent assembly techniques, and secondary support from the US Department of Energy Office of Basic Energy Sciences, Division of Materials Science and Engineering (award number DE-SC0002158) for the development of the semiconductor nanocrystal chemistry and the characterization of electrical conductivity. Electron microscopy research was performed while A.C.J.-P. held a National Research Council Research Associateship Award at the National Institute of Standards and Technology. We thank K. Yager (Brookhaven National Laboratory) for help with SAXS experiments. Work performed at the National Synchrotron Light Source I (Brookhaven National Laboratory) was supported by the US Department of Energy, Office of Basic Energy Sciences, under contract number DE-SC0012704. C.R.K. thanks the Stephen J. Angello Professorship for support. C.B.M. is grateful for the support of the Richard Perry University Professorship.

Author Contributions M.C., B.T.D. and C.B.M. conceived the idea for the study. M.C. prepared the samples and conducted initial characterization. A.C.J.-P. performed microscopy characterization and tomography reconstruction. B.D. and D.D. contributed to sample preparation and Voronoi analysis. V.V.T.D.-N. contributed to Voronoi analysis and Matlab programming. E.W. prepared electrical substrates and contributed to electrical characterization. M.C. and B.T.D. performed electrical characterization. A.A.H. supervised microscopy characterization. C.R.K. supervised electrical characterization. C.B.M. supervised the entire project. M.C. wrote the manuscript with contributions from all the authors.

Author Information Reprints and permissions information is available at www.nature.com/reprints. The authors declare no competing financial interests. Readers are welcome to comment on the online version of the paper. Correspondence and requests for materials should be addressed to C.B.M. (cbmurray@sas.upenn.edu).

METHODS

Synthesis of building blocks. Au nanocrystals are prepared according to ref. 29 with slight modifications. 1 mmol *tert*-butylamine-borane complex (97%, Sigma-Aldrich) is dissolved in oleylamine (80–90%, Acros Organics, 2 ml) and 1,2,3,4-tetrahydronaphthalene (tetralin, Acros Organics, 2 ml) by sonication. This solution is swiftly injected into a solution of $HAuCl_4$ (200 mg) in 20 ml oleylamine (80–90%, Acros Organics) and 20 ml 1,2,3,4-tetrahydronaphthalene (tetralin, Acros Organics) at room temperature (about 22 °C). Reduction occurs almost immediately, as shown by a change in colour from orange to dark red, but the reaction is left stirring in air for 1 h. The flask is then sealed and flushed with N_2, and the temperature is increased to 60 °C. At this point, 100 µl of 1-dodecanethiol (>98%, Sigma-Aldrich) is slowly added. At the end of the addition (after about 3 min), the flask is cooled and opened to the air. Particles are then purified by three rounds of precipitation in isopropanol/ethanol (3/1, 40 ml) and centrifugation (837.75 rad s^{-1}, 3 min), with dissolution in hexane after each step. Finally, particles are dissolved in hexane at a concentration of Au of about 5 g l^{-1}. For Ag/Au nanocrystals, 0.05 mmol of silver tetrafluoroborate were added to 2 ml Au nanocrystal solution and 1 mmol oleic acid, 1 mmol oleylamine and 1 mmol 1,2-hexadecanediol in 10 ml 1-octadecene (ODE), and the solution was heated under nitrogen gas to 180 °C for 5 min. Purification was the same as for Au nanocrystals.

Two steps are used to synthesize 5.5-nm zinc-blende CdSe nanocrystals. First, 3.5-nm CdSe cores are prepared; second, these cores are coated with additional CdSe by slow injection. The procedure is as follows. A cadmium oleate stock solution is prepared by dissolving CdO (1 mmol) in oleic acid (2.2 mmol) and 1-ODE at 270 °C until a clear solution is obtained. The concentration of Cd in the solution is 0.5×10^3 mol m^{-3}. 2 ml of this Cd stock solution are then mixed with 39 mg Se and 8 ml ODE in a 50-ml three-neck flask, and evacuated to <266.6 Pa at 110 °C for 30 min. After flushing with N_2, the flask is quickly (~50 °C min^{-1}) heated to 240 °C, and 6 ml of a solution of oleic acid/dioctylamine/ODE (1/1/2 in volume) are swiftly injected into the flask. The temperature drops upon injection and then recovers to 240 °C. 30 min after injection, the solution is heated further to 280 °C and a solution of Cd oleate stock (4 ml, 2 mmol) and Se/ODE (20 ml, 0.1×10^3 mol m^{-3}, prepared by dissolving Se in ODE at 280 °C for 4 h) is injected at 0.2 ml min^{-1} by using a syringe pump (New Era). At the end of the addition, the flask is cooled to room temperature and nanocrystals are purified by six rounds of precipitation in isopropanol/ethanol (3/1, 40 ml) and centrifugation (837.75 rad s^{-1}, 3 min) with dissolution in hexane after each step. Finally, nanocrystals are dissolved in hexane at a concentration of ~25 g l^{-1}.

6.5-nm PbSe nanocrystals are prepared following ref. 30 with some modifications. PbO (1 mmol) and oleic acid (2.5 mmol) are mixed in ODE (5 ml) and evacuated (<266.6 Pa) at 110 °C until a clear solution is formed (~1 h). After flushing with N_2, the solution is heated to 180 °C and 2 ml of a solution of trioctylphosphine selenide (TOPSe) are quickly injected into the flask. The TOPSe solution is prepared by dissolving Se powder in 90% trioctylphosphine to obtain a 1×10^3 mol m^{-3} solution containing 18 µl of diphenylphosphine in a glovebox (note that diphenylphosphine is extremely flammable in contact with air; take proper precautions when handling). The temperature drops to about 150 °C, is allowed to recover to 160 °C and is left there for 20 min. After cooling to room temperature, nanocrystals are purified by performing six rounds of precipitation in isopropanol/ethanol (3/1, 40 ml) and centrifugation (837.75 rad s^{-1}, 3 min) with dissolution in hexane after each step. Finally, PbSe nanocrystals are dissolved in hexane at a concentration of ~25 g l^{-1}.

Preparation of doped nanocrystal superlattices and ligand exchange. Doped nanocrystal superlattices are assembled at the air–liquid interface following an established procedure[14]. Dispersions of Au nanocrystals (~5 g l^{-1}) and CdSe or PbSe nanocrystals (~10 g l^{-1}) are mixed in a small plastic tube and the solvent evaporated using a gentle nitrogen flow. Then, 25 µl of hexane is added to redissolve the particles. This solution is then dropped onto the surface of 1.8 ml diethylene glycol (DEG) in a Teflon well (~1.5 cm × 1.5 cm × 0.9 cm). The well is covered with a glass slide to reduce the evaporation rate. After 30–60 min, the film forms and can be picked up with the appropriate substrate for characterization (for example, TEM grid, quartz piece, or patterned substrate for conductivity measurements).

A series of samples is prepared. For the initial screening of monolayers, a solution of CdSe nanocrystals diluted in hexane (1 to 2 by volume) and a solution of Au nanocrystals diluted in hexane (1 to 3 by volume). These stock solutions are mixed in the following volume ratios (CdSe/Au, µl/µl): 50/0; 50/5; 50/10; 50/15; 50/20. For the preparation of multilayers and for conductivity experiments, two solutions (CdSe or PbSe nanocrystals and Au nanocrystals) are mixed in the following volume ratios (CdSe or PbSe/Au, µl/µl): 30/0; 30/5; 30/25; 30/50; 0/50. After the film is deposited on the substrate, the film is dried under vacuum (at <3,000 Pa) overnight.

Ligand exchange is performed in two steps: *in situ* and solid exchange. The *in situ* exchange is performed by injecting 100 µl of a 0.4×10^3 mol m^{-3} solution of NH_4SCN in acetonitrile into the DEG layer while the nanocrystal film is still floating onto the DEG. The exchange is allowed to continue for 60 min or 15 min (for CdSe or PbSe, respectively) and then the films are transferred onto the substrate and evacuated (at <266.6 Pa) overnight. If the film is not thoroughly dry, it tends to delaminate during solid exchange. The solid exchange is performed by immersing the substrate with the film into a 0.4×10^3 mol m^{-3} solution of NH_4SCN in methanol for 30 s. Afterwards the film and substrate are rinsed in acetone. Fourier-transform infrared spectroscopy supports the exchange of the long oleic acid ligands with the compact SCN^-. All sample manipulations are performed in air.

Voronoi analysis. The procedure consists of extracting the signal originating from Au nanocrystals, taking advantage of the difference in contrast to filter out the CdSe nanocrystals. The Voronoi tessellations are performed using centroid information of the position of each particle, which is exported using the software ImageJ. In a typical Voronoi cell generation, the Voronoi space consists of a set of points closer to each (x, y) centroid than all other centroids. The Voronoi cell edges are generated by bisecting orthogonally the lines that connect two neighbouring centroids. This type of Delaunay triangulation, and histogram binning of the Voronoi cell areas, number of Voronoi cell edges, and centre-to-centre distances are performed using an in-house Matlab code and its "*Voronoi*" functions.

Code availability. The Voronoi tessellations generation code is freely available in a Github repository at https://github.com/vdoann/voronoi.

Characterization techniques. Substrates for electrical characterization consist of 20 nm Al_2O_3 grown by atomic-layer deposition on the surface of 250 nm thermal SiO_2 on heavily n-doped silicon wafers. Gold electrodes (10 nm) are deposited by thermal evaporation through a shadow mask. Channel lengths (L) and widths (W) range from 30 µm to 200 µm, with a constant W/L ratio of 15 for all devices.

Initial TEM characterization is performed on a JEOL JEM 1400 microscope operating at 120 kV, and on a JEOL JEM 2100 microscope operating at 200 kV. Samples are prepared using 300-mesh carbon-coated Cu grids (Ted Pella Inc.).

HAADF-STEM and EDS data are acquired using a probe-corrected Titan 80-300 microscope (FEI Co.) operated at 300 kV. The semiconvergence angle used to acquire EDS spectrum images is ~21 mrad. This angle is ~14 mrad or ~10 mrad for acquiring HAADF images, including those in the electron tomography tilt series. Several tilt series are acquired from both the Au–CdSe and Au/Ag–PbSe samples. Generally, a tilt range from -63 ± 5 degrees to $+63 \pm 5$ degrees is sampled at increments of 1.5 degrees or 2 degrees. The tilt series are processed using Inspect3D (FEI Co.); this includes alignment and reconstruction by the simultaneous iterative reconstruction technique. Three-dimensional visualizations are performed in Avizo (FEI Co.).

Ultraviolet–visible spectra are recorded in transmission mode on a Cary 5000 spectrophotometer at 2-nm spectral bandwidth. Small-angle X-ray data are collected with a multi-angle X-ray scattering system, using a Bruker FR591 rotating anode at 40 kV and 85 mA, Osmic confocal optics, Rigaku pinhole collimation, and a Bruker HiStar Multiwire detector.

TSAXS (transmission small-angle X-ray scattering) and GISAXS (grazing incidence small-angle X-ray scattering) measurements are performed at the X9 Beamline at the National Synchrotron Light Source I (Brookhaven National Laboratory). The beam-spot size is 50-µm tall and 200-µm wide. The beam energy is 13.5 keV; the sample-to-detector distance is set to 3 m; and detection is performed using a Mar charge-coupled device detector. Typical sampling times are 10 s for GISAXS measurements and 30 s for TSAXS measurements. These conditions appear to have no negative effects on the structures measured, despite multiple measurements. Two-dimensional detector images are analysed using GISAXS Shop (https://sites.google.com/site/byeongdu/software).

Room-temperature conductivity measurements are performed using a model 4156C semiconductor parameter analyser (Agilent) in combination with contacts made from a Karl Suss PM5 probe station mounted in a nitrogen glovebox. Conductivity shows only weak dependence on the channel length, as expected for a fixed W/L ratio. Values reported are calculated from 12 independent electrode pairs from two substrates, assuming the conductive channel to have dimensions equal to the channel's cross-section.

Temperature-dependent conductivity measurements are performed under vacuum (~133.3 µPa) in a Lakeshore Cryotonics (formerly Desert Cryogenics) probe station equipped with a model 4156C semiconductor parameter analyser. For measurements in this work, samples are cooled with liquid nitrogen and measurements are taken from 85 K to 300 K. Data shown in the main text are from a single channel, but similar results are obtained from other channels.

Certain commercial equipment and materials are identified in this paper in order to specify the experimental procedure adequately. In no case does such identification imply recommendations by the National Institute of Standards and Technology nor does it imply that the material or equipment identified is necessarily the best available for this purpose.

29. Peng, S. *et al.* A facile synthesis of monodisperse Au nanoparticles and their catalysis of CO oxidation. *Nano Research* **1,** 229–234 (2008).
30. Yu, W. W., Falkner, J. C., Shih, B. S. & Colvin, V. L. Preparation and characterization of monodisperse PbSe semiconductor nanocrystals in a noncoordinating solvent. *Chem. Mater.* **16,** 3318–3322 (2004).

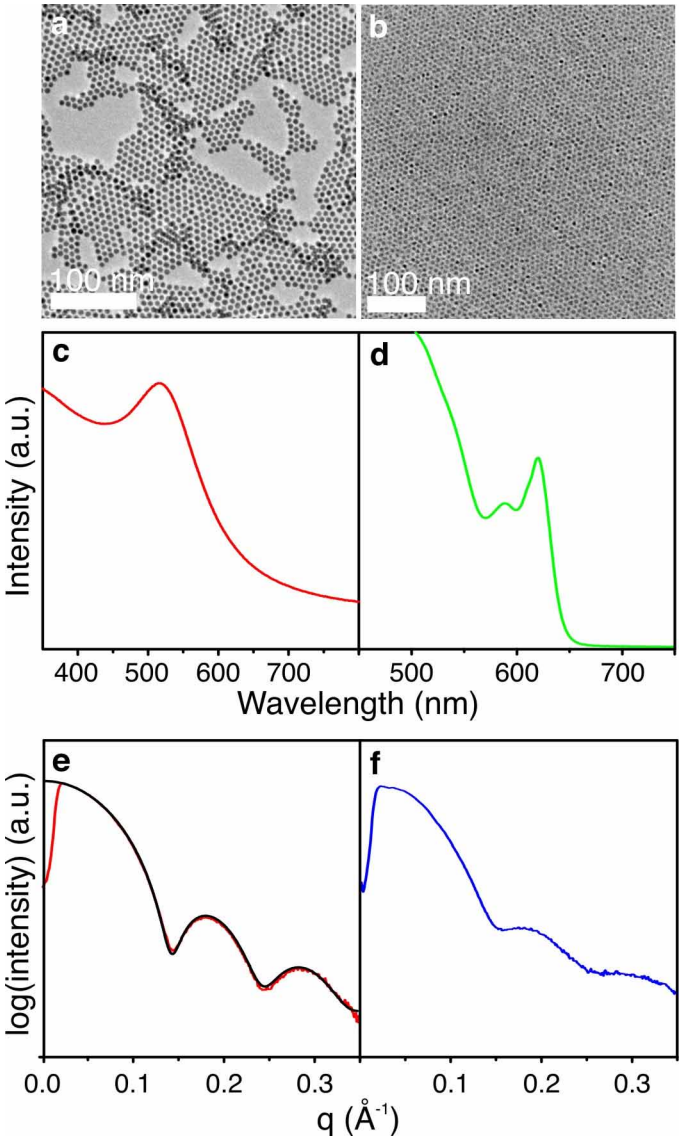

Extended Data Figure 1 | Characterization of starting building blocks. **a**, **b**, Representative TEM images; **c**, **d**, ultraviolet–visible spectra; **e**, **f**, small-angle X-ray scattering (SAXS) patterns, of Au nanocrystals (**a**, **c**, **e**) and CdSe nanocrystals (**b**, **d**, **f**). For Au, the SAXS data include the fit to particle size and size dispersion (solid black trace), providing an estimated particle diameter of 6.85 ± 0.45 nm (95% confidence, including organic ligand shell).

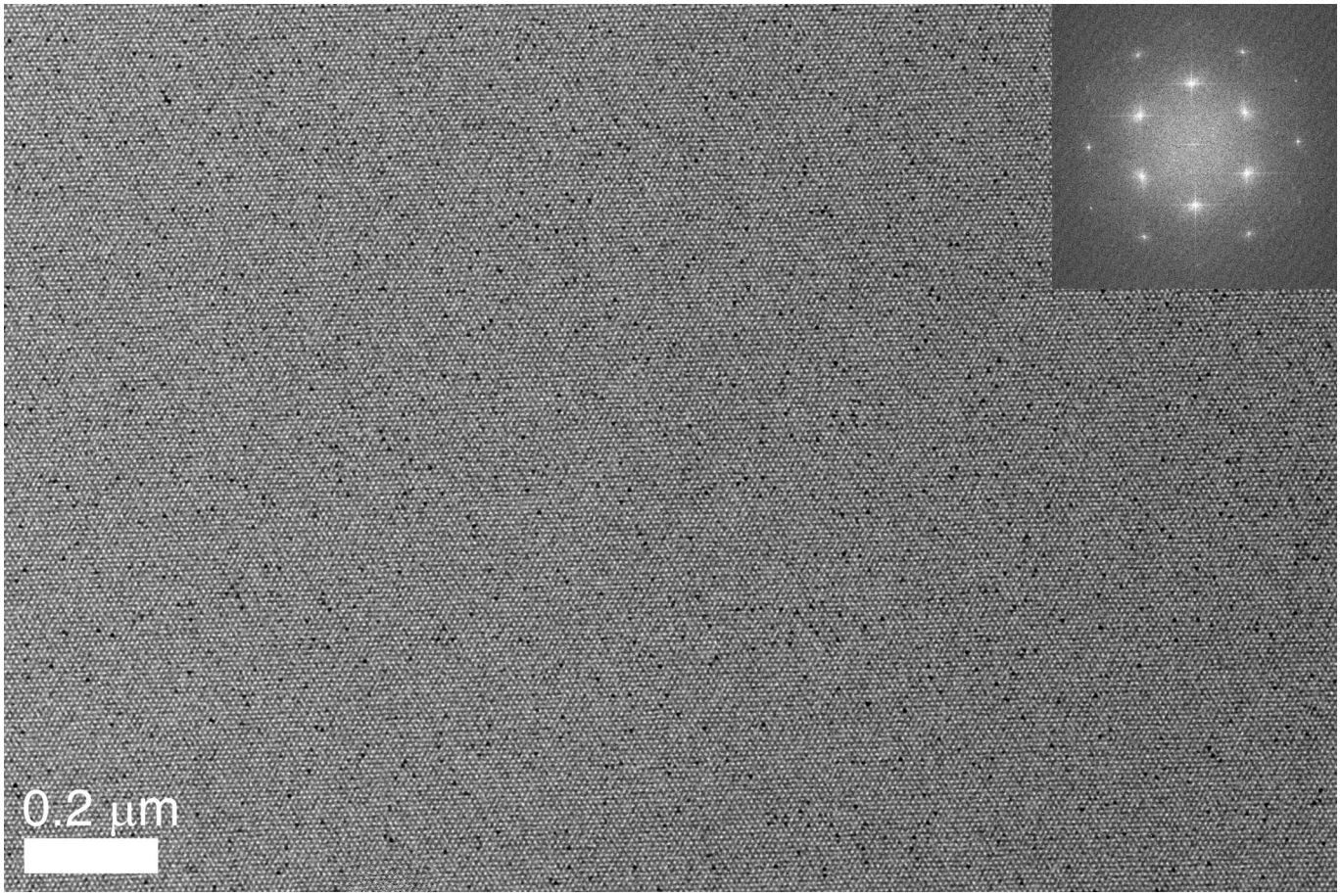

Extended Data Figure 2 | Long-range large-area ordering in doped nanocrystal superlattices. Low-magnification TEM image of CdSe superlattices doped with Au, showing the large areas (at least 5 μm^2) of ordered assemblies formed onto TEM grids. Inset, digital diffraction pattern showing the hexagonal long-range ordering in the superlattices.

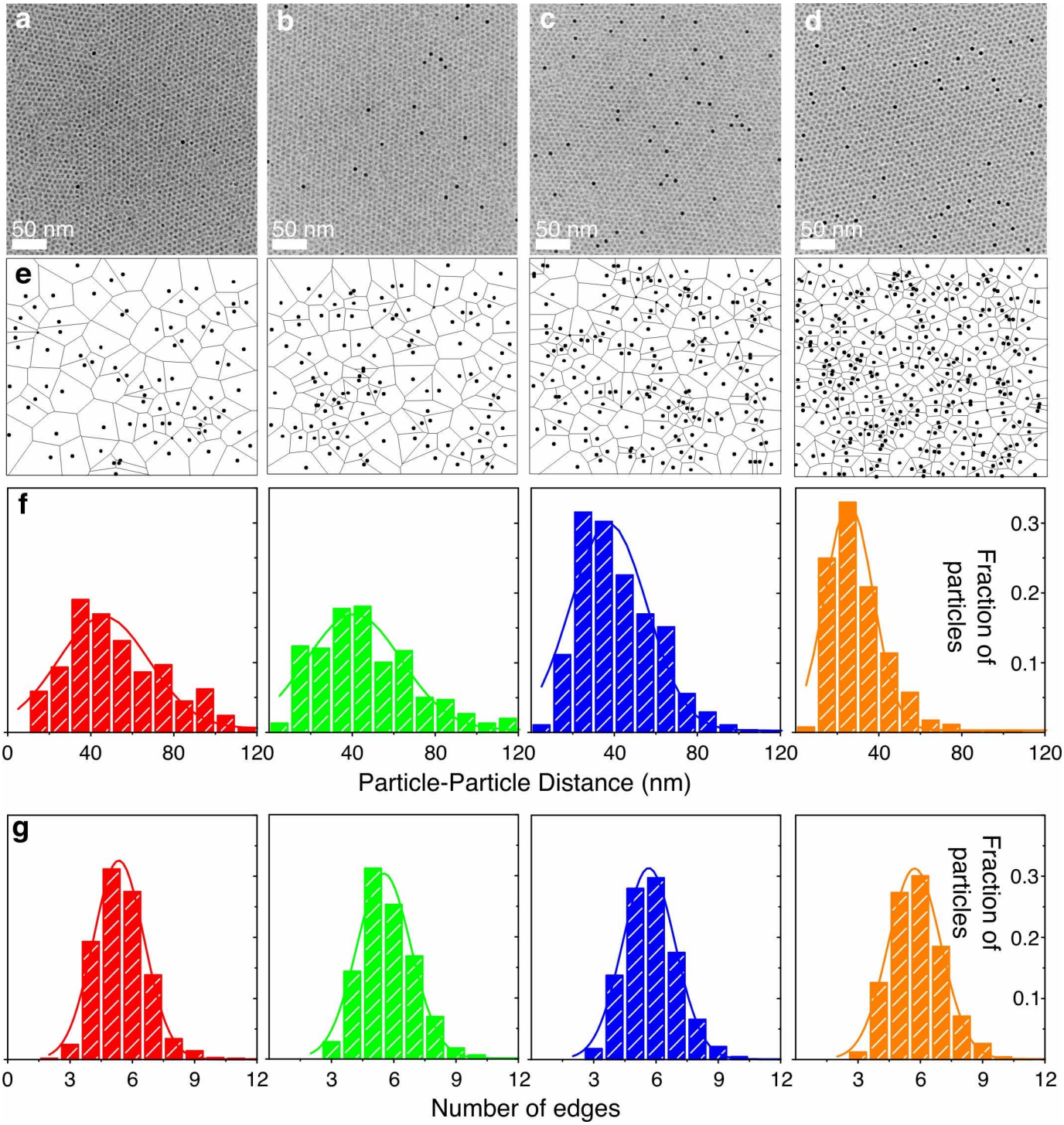

Extended Data Figure 3 | Voronoi analysis of doped monolayer superlattices. a–d, Representative TEM images of mixed Au/CdSe ordered monolayers with different densities of Au nanocrystals: **a**, 66 nanocrystals μm^{-2}; **b**, 128 nanocrystals μm^{-2}; **c**, 183 nanocrystals μm^{-2}; **d**, 317 nanocrystals μm^{-2}. **e**, Corresponding larger-area Voronoi diagrams. **f**, Associated particle–particle distance histograms. **g**, Average number of edges.

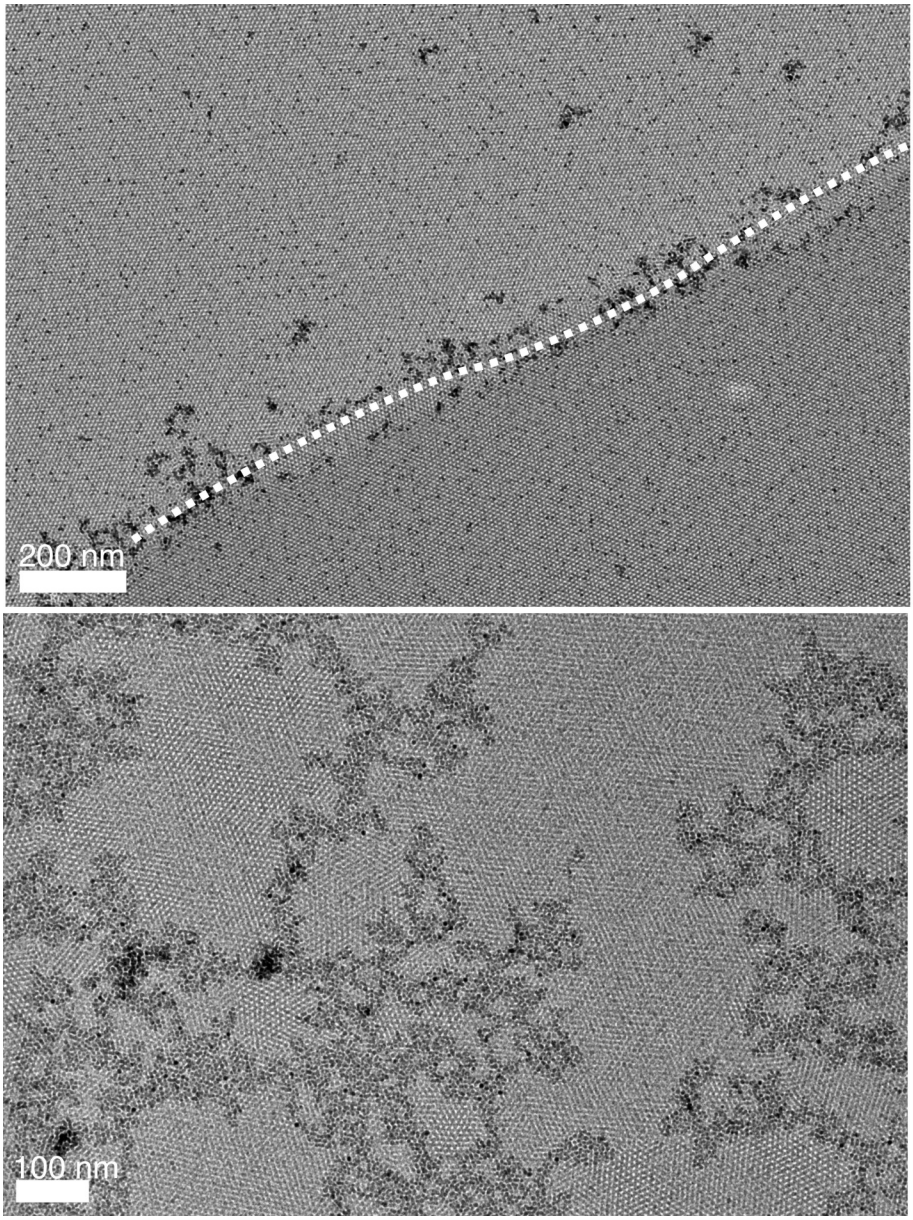

Extended Data Figure 4 | Segregation of dopants. Superlattices assembled from oleylamine-capped Au nanocrystals and oleic-acid-capped CdSe nanocrystals. Au nanocrystals tend to segregate and agglomerate at grain boundaries instead of mixing with CdSe nanocrystals. The grain boundary between two assembled regions of CdSe nanocrystals is highlighted by a dashed white line.

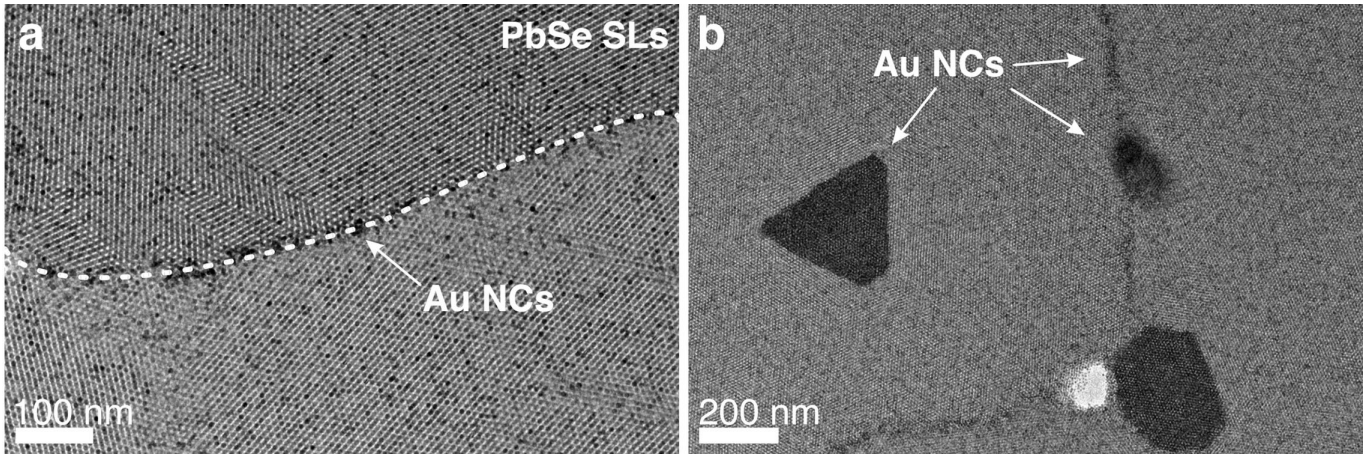

Extended Data Figure 5 | Segregation of Au nanocrystals owing to size mismatch. Assembly of 6.5-nm PbSe nanocrystals and 5.5-nm Au nanocrystals (NCs) at the liquid–air interface. Arrows point to grain boundaries or regions on top of the PbSe superlattices (SLs) where Au nanocrystals segregate preferentially.

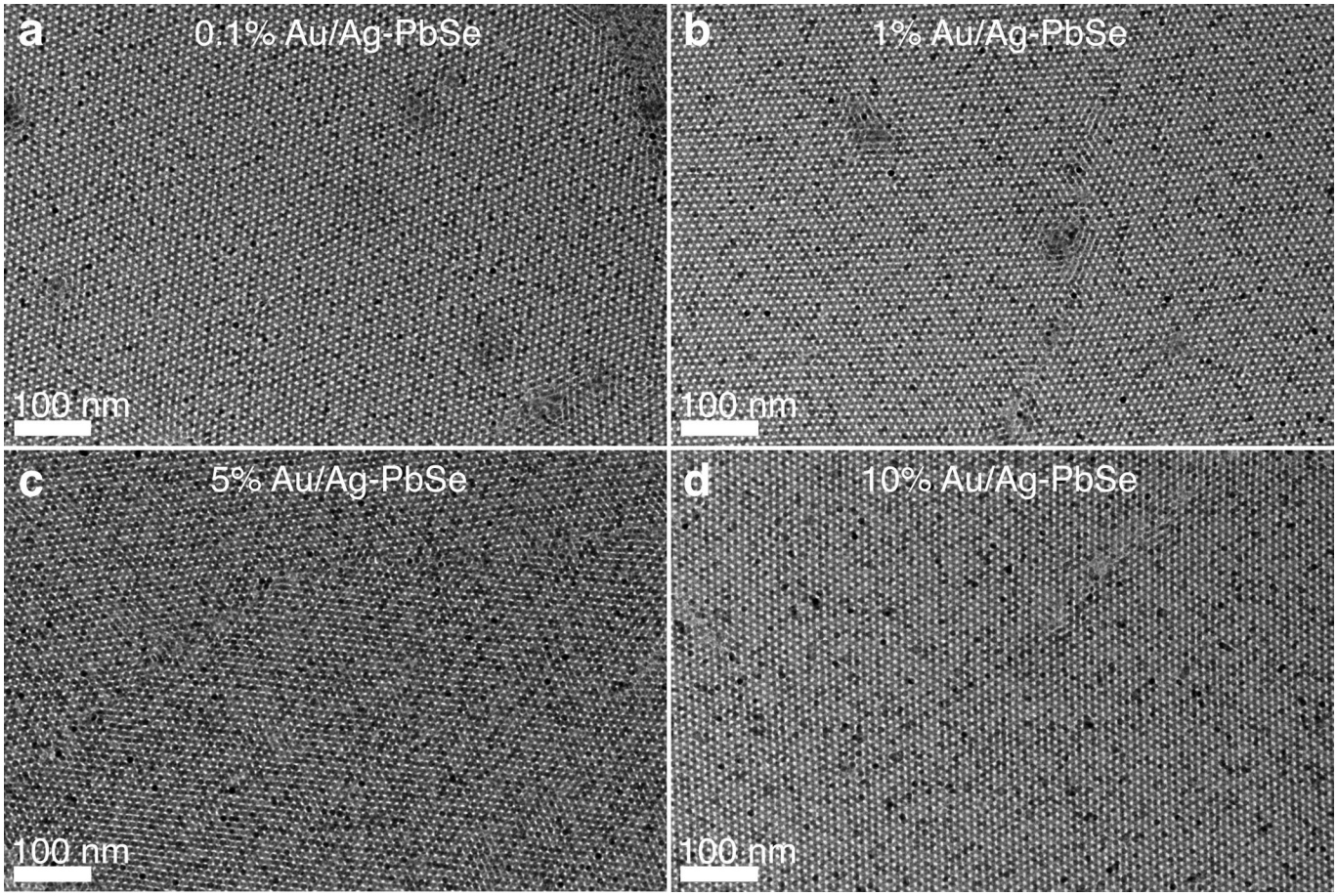

Extended Data Figure 6 | PbSe superlattices doped with Au/Ag nanocrystals. The images show the assembly of PbSe superlattices doped with different Au/Ag concentrations by volume at the liquid–air interface.

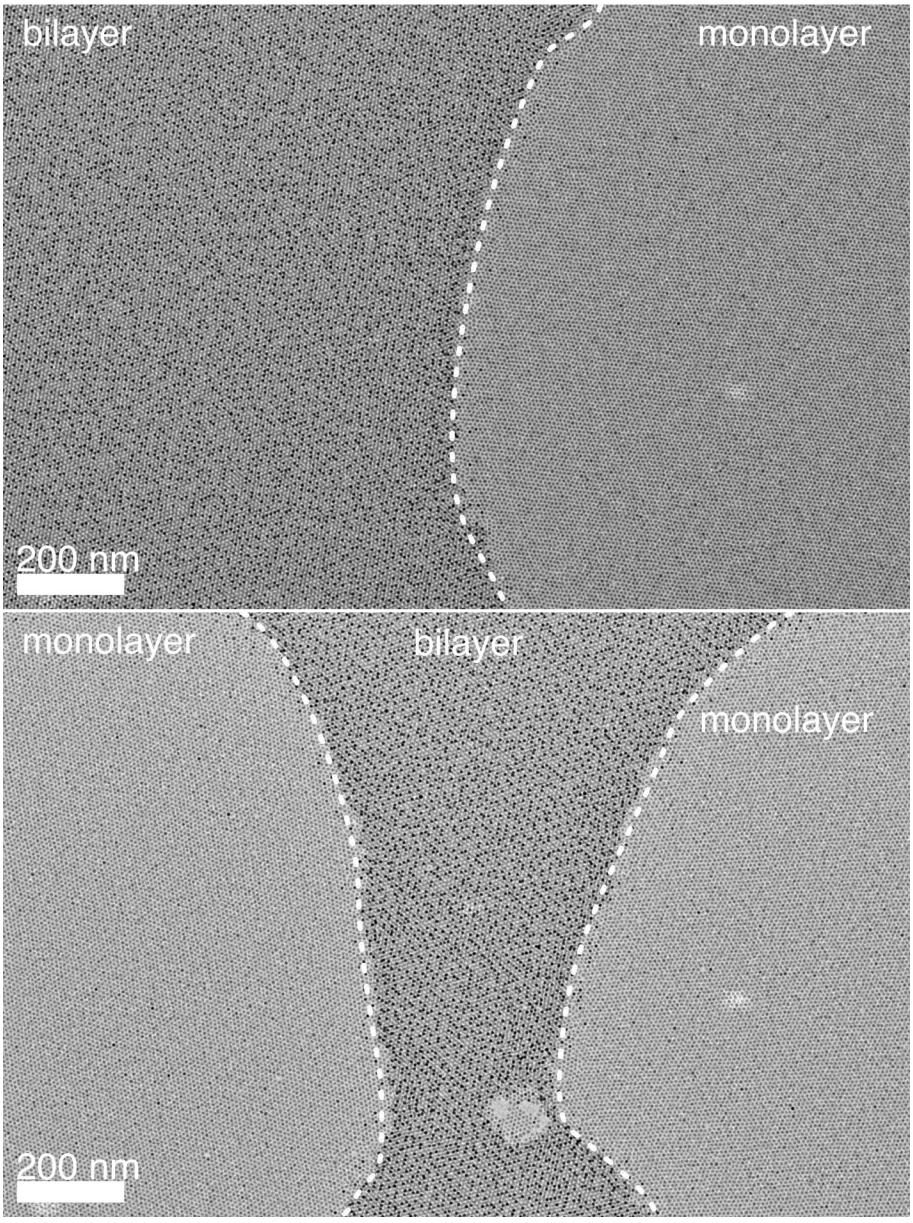

Extended Data Figure 7 | Segregation of dopants in multilayers. TEM images showing preferential segregation of Au nanocrystals to regions of CdSe multilayers rather than monolayers. Grain boundaries are highlighted with dashed white lines.

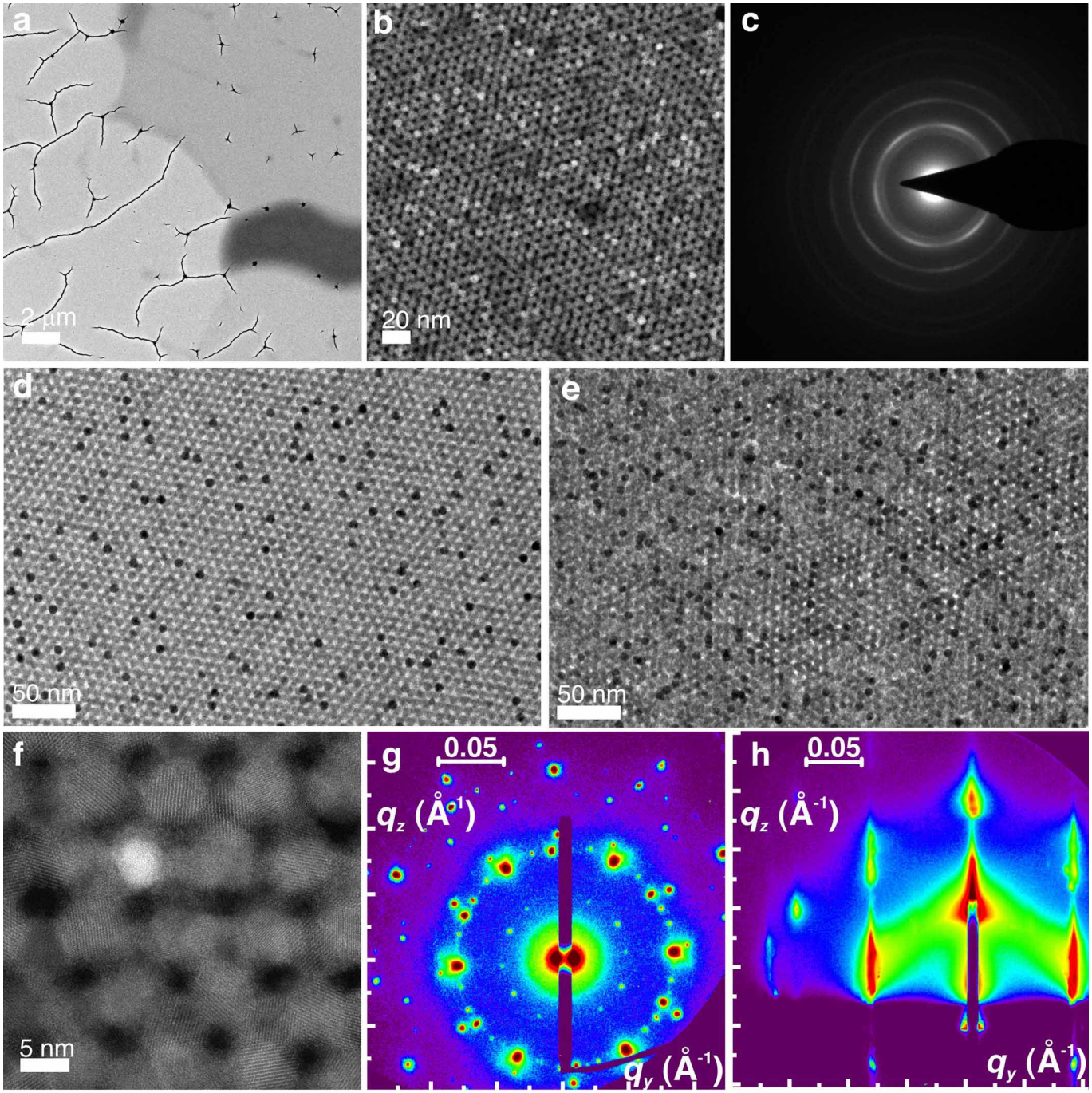

Extended Data Figure 8 | Characterization of ligand-exchanged doped superlattices. **a**, **b**, Representative TEM images of Au/Ag-doped PbSe films following ligand exchange of the long, alkyl ligands with compact thiocyanate ions. Extensive cracks are formed, especially where the grain boundaries were present. **c**, Selected area electron diffraction pattern of Au/Ag–PbSe assemblies, showing a low degree of preferential orientation of the crystallographic axes. **d**, **e**, Au–CdSe films before (**d**) and after (**e**) ligand exchange, showing that the order is preserved to a large extent, given the presence of hexagonal close-packed patches in the sample. **f**, High-resolution STEM of an Au/Ag–PbSe film after ligand exchange. **g**, **h**, TSAXS and GISAXS analysis of the films before (**g**) and after (**h**) ligand exchange.

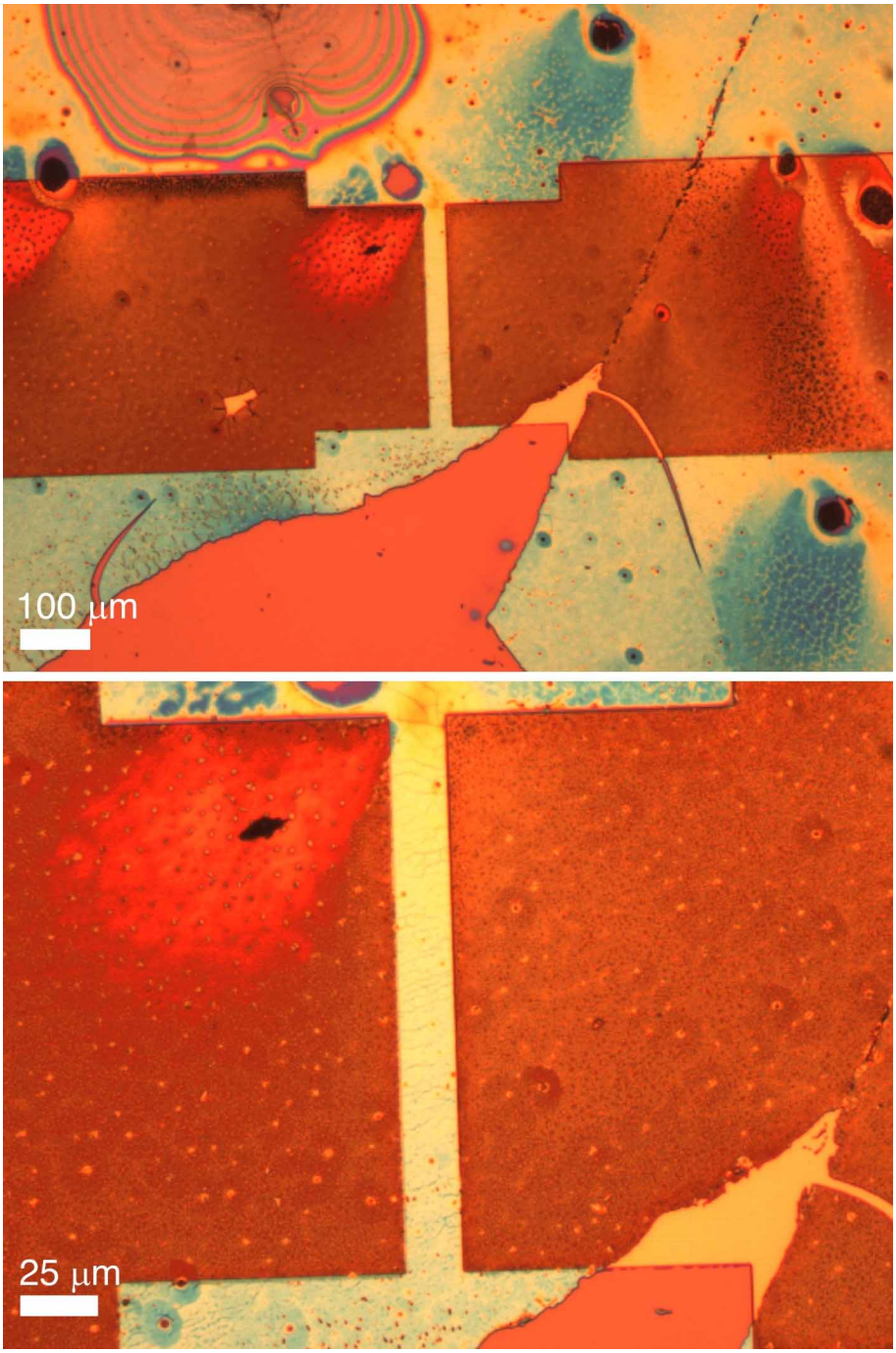

Extended Data Figure 9 | Substrates for conductivity measurements. Optical microscopy images of the patterned substrates covered with the doped superlattices for conductivity measurements.

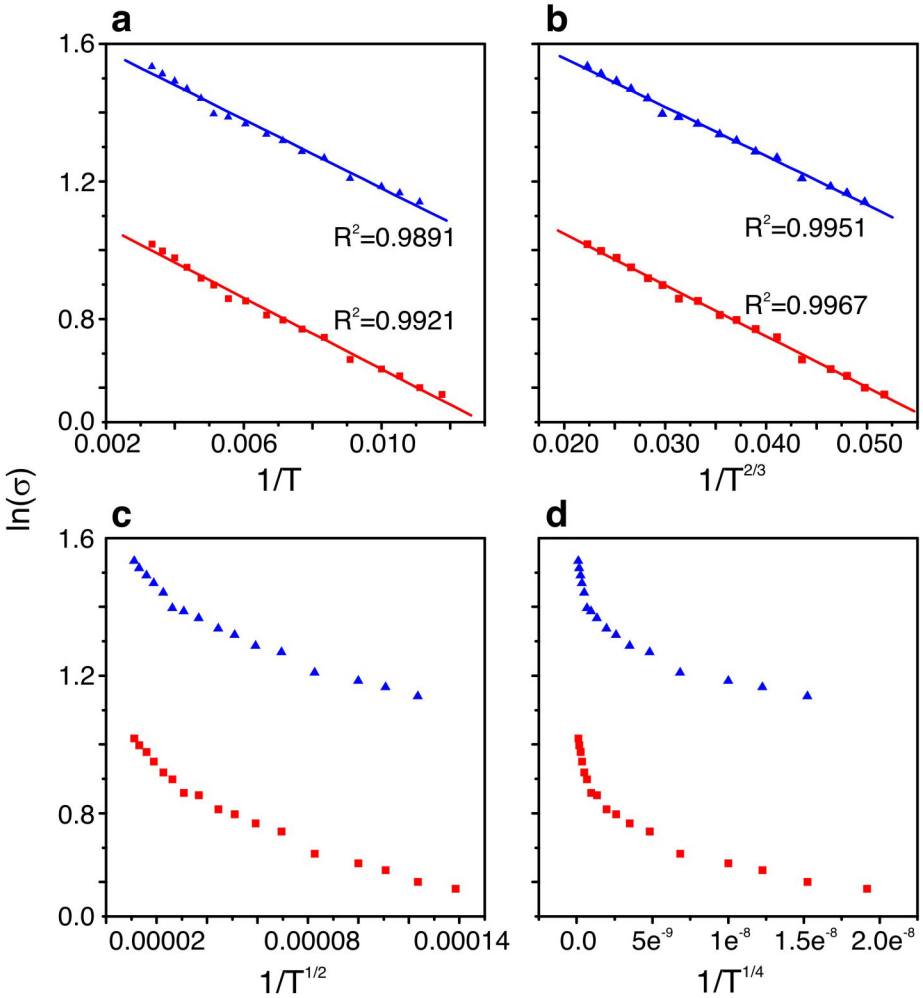

Extended Data Figure 10 | Temperature-dependent conductivity models. **a–d**, Fitting of different temperature-dependent conductivity models to data obtained for samples of PbSe doped with 16.5% Au/Ag. The best single fit out of several possibilities over the entire temperature range is a modified form of the Efros–Shklovskii variable-range hopping with $T^{-2/3}$ dependence, shown in **b**. The observation of this behaviour in sub-percolation doped superlattices is to be expected, because conductivity is constrained by hopping to non-nearest neighbours. The good fit obtained using the general T^{-1} expression for near-neighbour hopping, shown in **a**, not surprisingly still describes the system quite well, given that the composition is close to the percolation threshold. However, a reduced activation energy analysis also suggests that the transport behaviour is in best agreement with modified Efros–Shklovskii hopping. The original Efros–Shklovskii variable-range hopping dependence with $T^{-1/2}$ shown in **c** was found in the past to describe CdSe solids well; however, the presence of Au nanocrystal dopants clearly changes the behaviour in our system compared with the behaviour of pure quantum dot solids. The Mott variable-range hopping with a dependency of $T^{-1/4}$, shown in **d**, clearly does not describe the system, probably because of the increased density of states in the solid owing to the presence of the Au nanocrystal dopants.